Effect of the alkali *vs.* iron ratio on glass transition temperature and vibrational properties of synthetic basalt-like glasses

Michele Cassetta[1*], Beatrice Giannetta[2], Francesco Enrichi[1], Claudio Zaccone[2,3], Gino Mariotto[1], Marco Giarola[4], Luca Nodari[5], Marco Zanatta[6], Nicola Daldosso[1]

[1]*Department of Computer Sciences, University of Verona, I-37134 Verona, Italy*
[2]*Department of Biotechnology, University of Verona, I-37134 Verona, Italy*
[3]*National Institute of Geophysics and Volcanology, I-00143 Roma, Italy*
[4]*Centre for Technological Platform* (CPT)*, University of Verona, I-37134 Verona, Italy*
[5]*Institute of Condensed Matter Chemistry and Technologies for Energy, National Research Council (ICMATE-CNR), I-35127 Padova, Italy*
[6]*Department of Physics, University of Trento, I-38123 Trento, Italy.*

*corresponding author: michele.cassetta@univr.it

Volcanic eruptions generate huge amounts of material with a wide range of compositions and therefore different physicochemical properties. We present a combined Raman and calorimetric study carried out on four synthetic basaltic glasses with different alkali *vs.* iron ratio which spans the typical compositions of basalts on Earth. Differential scanning calorimetry shows that changes of this ratio modify the glass transition interval whereas Raman spectra allow to gain insight about the structure of the glass in the microscopic and macroscopic range. Indeed, our Raman analysis is extended from the high frequency region, characterized by the molecular peaks, to the very low frequency region where glasses exhibit the boson peak. Spectra show a variation of the non-bridging oxygens number that affects the medium range order of the glass and the network interconnections. In the considered substitution interval, the boson peak shape is conserved while its position shift upwards. This means that increasing the alkali *vs.* iron content the elastic medium hardens but it does not change nature. This study emphasizes the importance of considering the full-range spectra when analysing multicomponent or natural systems with small chemical variations.

39 ***Introduction***

40

41   The physical properties of silicate melts control the dynamics of magmatic processes and

42 consequently the eruptive behaviour of volcanoes [1–3]. However, from another point of view,

43 volcanic systems can be considered natural reservoirs offering a wide variety of raw materials for

44 applicative perspectives [4,5]. Indeed, the Earth volcanism provides itself the most abundant source

45 (about 70% of the crust) of naturally-prone to application silicate melts, such as basalts (see Ref. [6]

46 and literature therein). Small chemical corrections or else doping of this pristine material allow the

47 tuning of its physical and mechanical properties, thus constituting a cheap source of materials for

48 specific applications (*i.e.* glass-ceramics, fibres, geo-grids, inertizing matrices or heat insulators [6]).

49   Iron oxides are among the major constituents of basalts. They are characterized by a dual role,

50 depending on their valence state: network former (NF) as Fe^{3+}, and network modifier (NM) as Fe^{2+}.

51 Strongly affected by particular condition such as temperature, pressure and oxygen fugacity, Fe^{3+}

52 could originate a range of coordinated structures from 4-fold (^{IV}) to 6-fold (^{VI}), deeply influencing

53 the melt structure, thermal properties and rheology [7–14]. Moreover, $Fe^{3+}/\Sigma Fe$ (where ΣFe is the

54 total Fe content) is strongly influenced not only by the redox condition during vitrification (*i.e.*,

55 oxygen fugacity), but also by the glass chemistry itself [9]. The discrimination between Fe^{3+} as

56 network forming (tetrahedral, $^{IV}Fe^{3+}$) and network modifying (octahedral $^{VI}Fe^{3+}$) is a fairly

57 controversial and highly debated topic [15–17]. In justifying poor-resolved experimental data,

58 suggesting the presence of Fe^{3+} as NM cations, [10,16] evidence of $^{V}Fe^{3+}$ in a Fe_2O_3-doped soda-lime

59 silicate glass (in discrete site geometries such as square planar or trigonal bipyramidal). Following,

60 the average Fe^{3+} coordination number was found to varies from four- to six-fold in function of the

61 alkali and alkaline earth involved in the glass network. Of particular interest is that $^{IV}Fe^{3+}$ is stabilized

62 by larger alkali and smaller alkaline earth, while $^{V\text{-}VI}Fe^{3+}$ are stabilized by smaller alkali and larger

63 alkaline earth. Thus, it is worth to note that the ionic radius ratio between alkalis and alkaline earths

64 mirrors their antagonistic effects on Fe^{3+} coordination which seems to be the result of space-charge

65 effects [18]. According to the above observations, it is reasonable to assume that iron Fe^{3+}

66 coordination lies in a continuous distribution between four- and six-fold as function of glass

67 composition. Thus, addressing how iron and alkali ratio affects the glass structure is essential in both

68 material sciences [19] and geosciences [20].

69   Among the possible spectroscopic techniques [21–23], Raman spectroscopy has been proven

70 particularly successful in providing an effective, fast, and non-invasive way to obtain structural and

71 dynamical information on microscopic region of the sample (micro-Raman spectroscopy), without

72 the need of complex preparation procedures [13,24,25]. Most of the Raman analyses are usually

73 limited to region above ~200 cm^{-1}, which provides information on the molecular dynamics. A way

74 for indexing the structural information from the Raman spectrum is the Raman parameter (R_p), which

75 is the ratio between the integrated areas (or of the maximum spectral amplitudes) of the different

76 frequency regions [26–28]. However, the glass polymerization degree is commonly retrieved from

77 the deconvolution of specific Raman signatures, nominally the Q^n species in the 800-1250 cm^{-1} (high-

78 ω) [24,26]. This approach is used to identify n, the ratio of the bridging oxygen for each network

79 former atoms [29]. The high-ω bell is fitted with different gaussian functions and n is the ratio

80 between the area of the i-th gaussian and the total area of the peak.

81 Conversely, the spectral region below 200 cm^1 (low-ω) is usually forbidden to standard

82 instruments even though it holds key information on the mesoscopic nature of disordered materials.

83 Indeed, the Raman spectrum of a glass below 200 cm^{-1} is characterized by a broad peak known as

84 boson peak (BP). This spectral feature is due to an excess of vibrational modes [30] in the vibrational

85 density of states (VDoS) above the ω^2 Debye prediction. This excess results into a broad bump in the

86 reduced VDoS, $g(\omega)/\omega^2$. Despite its origin still represents matter of discussion, the BP is largely

87 endorsed as a universal fingerprint of the disorder [31–35] and is intimately related to the macroscopic

88 elastic and viscous properties [36], thermal conductivity and specific heat of glasses [37]. Indeed,

89 experimental investigations of the BP behaviour, in terms of both thermodynamic [38–43] and

90 chemistry [6,44,45], draw a coherent picture: the higher the disorder of the system (the more the glass

91 network undergoes perturbation), the higher the shift [46] of its maximum position ω_{BP}. This upwards

92 shift of ω_{BP} is usually accompanied by a decrease of the peak intensity. However, performing an

93 appropriate scaling procedure in terms of ω/ω_{BP}, spectra measured as a function of temperature [38]

94 pressure [47] or density [48] go one on the top of another so that a master curve is defined. This

95 scaling shows that the BP spectral shape is uniform whilst its intensity variation is only an apparent

96 effect due to the shift. In particular, in multicomponent systems where the evolution is marked by an

97 atomic species, the breaking of the scaling underlies a change in the elastic properties of the medium

98 and a "chemical limit" between two different glassy vibrational configurations. Above such a limit,

99 the glass experiences a redistribution of the collective modes in the VDoS that may be due to subtle

100 structural modifications [6].

101 This work aims at addressing how small fluctuations of the iron oxide (FeO$_{(t)}$) and alkali

102 contents in basaltic-like glasses shape their structural and thermodynamical properties. In this regard,

103 we investigated the effects of small variations of alkali oxides (M$_2$O, M = Na, K) and FeO$_{(t)}$ with

104 particular focus on its oxidation state retrieved by Mössbauer spectroscopy, on a set of four basaltic

105 glasses by means of Raman spectroscopy and differential scanning calorimetry (DSC). Samples are

106 obtained by keeping constant the concentration of the other major elements, the alkali ratio (K# ~

107   0.24 ± 0.02) and the acidity modulus ($M_a \sim 4.7 \pm 0.1$). These parameters are ideal for the continuous

108   basalt fibre production. The chemical variation impacts on the $Fe^{3+}/\Sigma Fe$ and directly affects the glass

109   structure, the glass transition temperature, and the viscosity of the melt [6,49,50].

110

111   *Experiments*

112   The four basaltic-like glasses (B1-B4) span the typical compositions of basalts on Earth [51].

113   They were synthesized by melt quenching starting from commercial grade oxide and carbonate

114   powders of Na_2CO_3, K_2CO_3, $CaCO_3$, MgO, Mn_3O_4, Fe_2O_3, $(NH_4)H_2PO_4$, Al_2O_3, TiO_2, and SiO_2

115   (purchased by Sigma Aldrich). Powders were weighted, mixed and melted in a Pt crucible at 1770 K

116   in muffle furnace for two hours and then quenched in air. The obtained glass was milled in a

117   zirconium ball mill, to ensure its homogenization, and then further melted for two hours. The final

118   product was casted on a Cu sheet and left to quench at room temperature. To test the calorimetric

119   determinations, we measured the natural trachybasalt from 122 B.C. Plinian eruption of Etna volcano,

120   Italy [52] (glass and chemical data was provided by Ref. [53]). For sake of clarity, we will refer to

121   the sample as B1, B2, B3, B4 and E122.

122   The resulting glasses were characterized by an electron microprobe analyzer (EMPA) JEOL

123   JXA-8900RL set at 15 kV acceleration voltage. The chemical composition of the studied glasses,

124   obtained by probing 10 points for each sample is reported in table 1. The uncertainty on the

125   composition is < 4.5%. No significant changes were observed between nominal and measured

126   composition.

127   The amorphous state of the glasses was verified trough the X-ray diffraction XRD patterns

128   reported in Fig. S1.

129   Thermal analysis was carried out using a simultaneous thermogravimetric and DSC analyzer

130   (TGA-DSC 3+, Mettler Toledo). Polished glass chips ($\sim$ 80 mg) of each sample were placed in an

131   alumina crucible and heated from 300 to 1070 K at 20 K min^{-1} under air with a flow rate of 100 mL

132   min^{-1}, to erase the thermal history of the sample. The temperature was then decreased to 470 K with

133   a cooling rate of 10 K min^{-1} and then heated with the same rate up to 1070 K. As expected, no change

134   in sample weight was observed throughout the heat treatment. This procedure satisfies the enthalpy-

135   matching principle and defines the onset of the glass transition (T^{onset}) as fictive temperature (T_f) [54],

136   Fig. 1. T_f was then identified as the intersection between the tangent to heat flow curve in the glassy

137   state and that to the inflection point in the glass transition interval. When the sample experiences the

138   glass transition with a heating rate of 10 K min^{-1}, the viscosity at T_f is 10^{12} Pa s so that $T_f = T_g$, the

139   glass transition temperature (see Ref. [54] and literature therein).

Raman measurements were carried out in backscattering geometry by a micro-Raman spectrometer Horiba Jobin-Yvon model T-64000 with three holographic gratings (1800 lines/mm), set in double subtractive/single configuration and coupled with a CCD detector having 1024×256 pixels and cooled by liquid nitrogen. The 514.5 nm line was provided by a mixed Ar-Kr ion gas laser (Spectra Physics, Satellite 2018 RM). Experimental conditions are the same as in Ref. [6]. Samples were visually inspected with the microscope ($50\times$ objective, having numerical aperture NA = 0.75) before and after the measurements to check the potential occurrence of micrometric alterations. Stokes spectra were acquired in the frequency region between 10 and 1300 cm^{-1}, with an average spectral resolution of about 0.6 cm^{-1}/pixel. Spectra were collected both in parallel (HH) and crossed (HV) polarization.

Mössbauer spectroscopy (MS) was carried out on a conventional constant-acceleration spectrometer, with a room-temperature Rh matrix ^{57}Co source, nominal strength 1850 MBq. The sample, ~80 mg, was gently crushed, dispersed in petrol jelly, and placed on a sample-holder of 2 cm diameter. Effects due to thickness were checked [55] and found to be negligible. The spectra were fitted to Lorentzian line shape with the statistical best fit evaluated by the reduced χ^2 method. The procedure was performed by using Recoil software [56]. The hyperfine parameters were obtained using the standard least-square minimization technique: isomer shift (δ), quadrupole splitting (Δ) and half linewidth at half maximum (Γ_+) are expressed in mm s^{-1}, while the relative area (A) in %. Alternative fitting, based on distribution of hyperfine parameters (Voigt-based Fitting, VBF) was attempted. VBF did not yield to significatively different results in term of $Fe^{3+}/\Sigma Fe$ and on sites parameters from the Lorentzian line shape one. Concerning the $Fe^{3+}/\Sigma Fe$ evaluation, it was assumed that Fe^{3+} and Fe^{2+} have the same recoil-free fraction. Considering the relative huge error that affects the areas evaluation, such approximation can be considered acceptable.

Results and discussion

The elements variation is limited in the frame of the alkali-iron substitution including the variation of the Fe oxidation state expressed by the $Fe^{3+}/\Sigma Fe$. Moreover, K_2O varies from 3.0 to 1.1 wt.% whereas Na_2O from 5.0 to 2.5 wt.%. The K# ratio (K# is expressed in mol basis) is quite constant among the samples ($0.23 \lesssim K\# \lesssim 0.26$). Conversely, the ratio between total iron oxide ($FeO_{(t)}$) and total alkali [$FeO_{(t)}/(FeO_{(t)}+Na_2O+K_2O$], expressed in mol basis, varies from 0.51 (B1) to 0.76 (B4), (Table 1).

Figure 1 (a) shows the DSC measurement of the glass E122, depicting the procedure used to determine the T_g of studied glasses as discussed above. The T^{onset} measured in E122 glass provides a

174 T_g = 915 K. Table 1 shows that T_g generally increases as $FeO_{(t)}$ replaces the total alkali, from 912 K

175 in B1 to 930 K in B4. The values of T^{peak} shows the same trend.

176
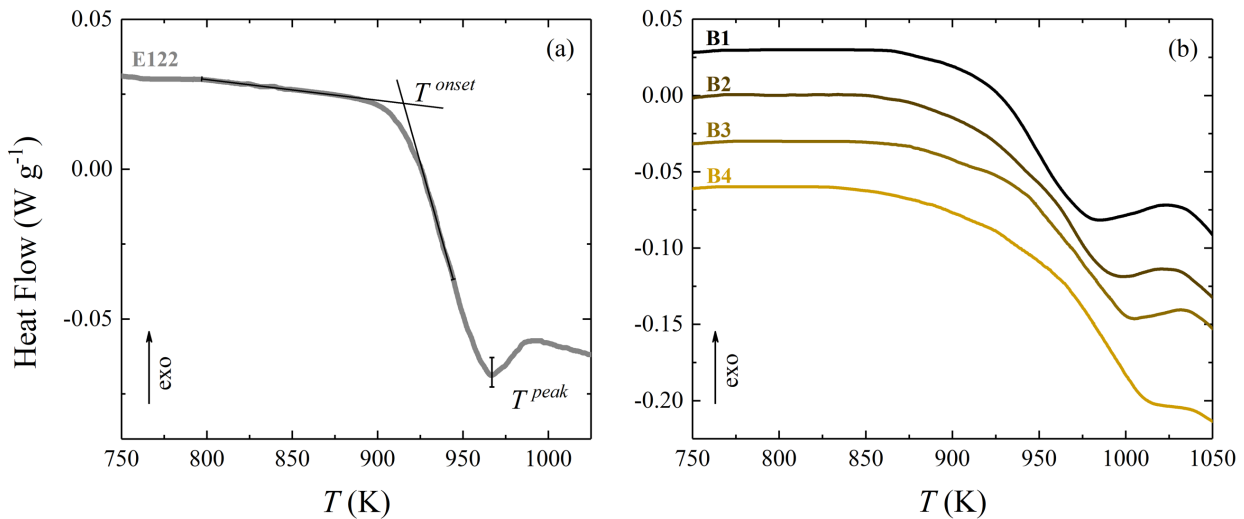
177

178 **Figure 1.** (a) Heat flow as a function of temperature for the E122 glass. Measurement is done across the glass transition
179 with a heating rate of 10 K min⁻¹. The sample was previously cooled at 10 K min⁻¹. The two glass transition temperatures
180 are the T^{onset}, (intersection of the two dashed lines) and T^{peak}, marked by the heat flow drop at the beginning of the
181 supercooled liquid region) see text. (b) Heat flow as a function of temperature of B1, B2, B3, B4 synthetic basalts.

182

183   The Mössbauer spectra (see Fig. S2) of basaltic glasses are characterized by broad and

184 asymmetric absorptions in the 0-2 mm s⁻¹ range, typical for Fe^{3+} and Fe^{2+} nuclei in paramagnetic

185 regime. The broadening of the absorptions is clearly imputable to the glassy nature of the sample and,

186 consequently, represents the superimposition of different ferric or ferrous sites characterized by

187 slightly different chemical environment. In general, the spectra were fitted by means of three different

188 subcomponents: two doublets ascribable to ferric sites and one due to ferrous one. The two ferric

189 doublets show δ and Δ values typical of distorted octahedral environments, differing each other for

190 the degree of distortion. Also, the ferrous component has parameters compatible with those of

191 distorted octahedral sites in glassy matrix. The quite huge half linewidth at half maximum reflects

192 the occupation of a large array of different geometries and coordination size polyhedral [20]. The so

193 obtained hyperfine parameters, reported in Table S1, are consistent with the literature [20,57].

194   The $Fe^{3+}/\Sigma Fe$ ratio, recalculated according to Mössbauer data, ranges from 0.72 (for the

195 trachybasalt glass E122) to 0.79 (for the iron-rich glass B3). The recalculated wt.% of Fe-oxides using

196 the $Fe^{3+}/\Sigma Fe_{(Mössbauer)}$, were found to vary from 7.0 (B1) to 10.2 wt.% (B4) for Fe_2O_3, and from 1.2

197 (B3) to 2.0 (B4) wt.% for Fe_2O_3.

198

199

	E122	B1	B2	B3	B4
SiO_2	49.4	49.6	49.6	49.7	49.7
TiO_2	1.7	1.6	1.6	1.6	1.6
Al_2O_3	18.8	16.0	16.0	16.1	16.6
$FeO_{(t)}$	9.5	8.5	9.4	10.3	12.3
MnO	-	0.2	0.2	0.2	0.3
MgO	3.6	6.0	5.9	5.9	6.0
CaO	9.2	8.0	7.8	7.6	7.7
Na_2O	4.1	5.0	4.5	4.0	2.5
K_2O	1.7	3.0	2.5	2.1	1.1
P_2O_5	-	0.8	0.8	0.8	0.8
$Fe^{3+}/\Sigma Fe$ (Mössbauer)	0.72	0.75	0.77	0.79	0.75
K#	0.21	0.28	0.27	0.26	0.23
$[FeO_{(t)}/(FeO_{(t)}+Na_2O+K_2O)]$	0.61	0.51	0.57	0.62	0.76
T_g (K)	915	912	919	921	930

Table 1 Chemical composition of the investigated glasses in wt% obtained by EMPA analysis (B1 nominal composition), $Fe^{3+}/\Sigma Fe$ measured by Mössbauer spectroscopy, K# = $[(K_2O)/(K_2O+Na_2O)]$ in mol basis, total iron ($FeO_{(t)}$) and total alkali oxides ratio $[FeO_{(t)}/(FeO_{(t)}+Na_2O+K_2O)]$ in mol. basis and T_g measured as explained in the text.

The whole evaluation of the HH Raman spectra was done by applying the Long-correction for the temperature and excitation line effect,

$$I(\omega) = I^{obs}\{\omega_0^3\, \omega\, [1 - \exp(-hc\omega/k_B T)]/(\omega_0 - \omega)^4\} \qquad (1)$$

where h is the Planck constant, k_B the Boltzmann constant, c the speed of light, T is the absolute temperature in K, ω_0 the frequency of the incident laser light (514.532 nm, ω_0 = 19435.1 cm^{-1}), and ω the observed frequency in cm^{-1}. Spectral intensities were normalized to the total area integrated from 200 to 1250 cm^{-1}. The data-treatment is reported in Fig. S3.

Figure 2 shows the HH spectra in the 200-1250 cm^{-1}. Starting from the lower frequency features, the spectra of glasses with decreasing alkali and increasing Fe contents (from B1 to B4) show a gradual intensity increase of the R band tail up to ~ 460 cm^{-1}, the position of the D_1 band maximum shift downwards from 495 to 486 cm^{-1} whilst the D_2 shoulder at about 570 cm^{-1} decreases its intensity. The different bands are originated by the geometry and local topology of the tetrahedrally coordinated cations (T) [58]. The R band is ascribed to the vibrations of 6-memberd rings [59], and the D_1 band is originated by the rocking and symmetric bending modes of bridging oxygens from 4-membered silica-tetrahedral rings [60,61]. Different T-O-T average bond angles, force constant and T-O average distance cause the shift of this band, whereas the different proportions between 4- and higher-member rings cause its intensity variations [62]. In our case, as $FeO_{(t)}$ replaces alkalis oxides (*i.e.*, going from B1 to B4), the observed behaviour indicates a decrease of the number of 4-membered rings thus

224   favouring the formation of higher-membered rings with wider angles. Finally, the D_2 shoulder is the

225   result of 3-membered rings network-decoupled planar motions. Its behaviour is strongly affected by

226   the strength of the bonds (*i.e.*, strong for Si atoms and weak for Al) [59]. Thus, its intensity decrease

227   is probably due to a weakening of the bonds induced by the increasing iron content, perhaps in the

228   form of Fe^{3+}. This effect should also cause an increase of the Q^4 species. Generally, this phenomenon

229   is observed in basaltic glasses having slight variation of major elements (as well as with variable

230     $Fe^{3+}/\Sigma Fe$) [13] than, we can safely relate this variation only to the increasing iron content. The general

231   picture is in line with that reported for iron-bearing diopsidic glasses [63].

232
233
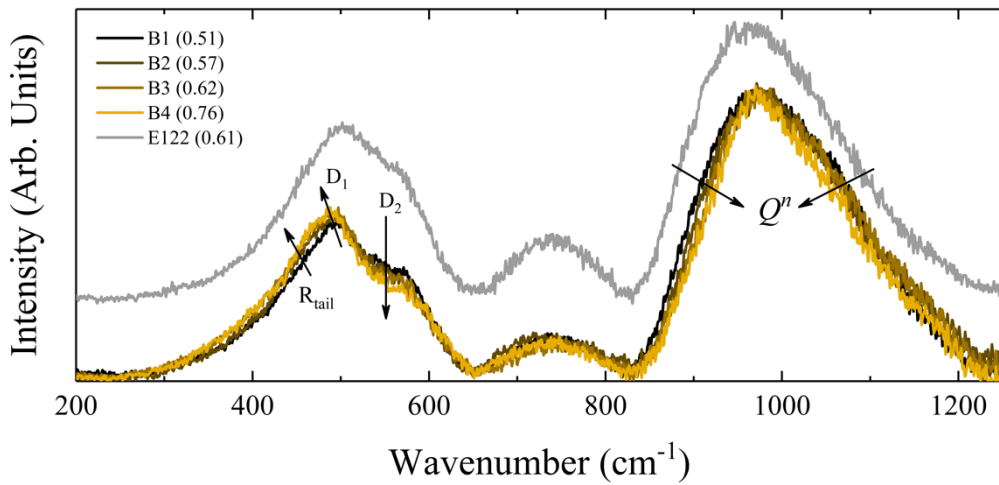
234
235 **Figure 2**. Long-corrected, HH polarized Raman spectra of the four basaltic-like glasses with increasing $FeO_{(t)}$ and
236 decreasing alkali oxides contents, from B1 to B4 respectively. E122 glass spectra is also reported in grey and displaced
237 upward for clarity. The ratios between $FeO_{(t)}$ and total alkali oxides are reported in brackets (see also table 1). The
238 arrows show the behaviour of the R tail, of the D_1 and D_2 bands, and of the TO_n peak (Q^n).

239

240   The high-ω (850–1250 cm^{-1}) region is dominated by a broad peak convolution of TO_4

241   tetrahedra modes. The contribution of the different T-units can be extracted by fitting the peak with

242   *n*-Gaussians components, namely the Q^n species, where *n* stands for *number of bridging oxygens* [64].

243   These Gaussian components control the intensity centred at about 850, 900, 1100, and 1150 cm^{-1}, for

244   the Q^1, Q^2, Q^3, and Q^4, respectively [29,60,65] and their relative intensity is controlled by the

245   chemical species forming the network. Moreover, the high-ω includes also the Fe^{3+} band, centred at

246   ~ 970 cm^{-1} and originated by the fourfold coordinated $^{IV}Fe^{3+}$-O bond stretching [22,66,67]. Further

247   studies claim that its origin is the result of merged signals from the $^{VI}Fe^{3+}$-O stretching in the glass

248   network and the Si-O stretching from Q^2 units (see Ref. [25] and literature therein). Even though the

249   interpretation of its behaviour is not trivial (starting from the assumption that its frequency variation

250   is negligible, unlike its intensity [68]), literature unanimously agrees that it can be used as a probe to

251   infer the iron oxidation state [13,24,25,50,67,69–71].

Having in mind the above discussion, here we follow the usual fitting procedure (with four Q-components) but adding a supplemental Fe^{3+} band centred at about 970 cm^{-1}. This further component is decoupled both from the Q^2 and Q^3 units. The deconvolution procedure was set by constraining both the full width at half maximum (FWHM) and the Raman shift of the Gaussian components to vary respectively within ± 20 and ± 5 cm^{-1} from the initially assigned values. The results are shown in Figure 3. Of course, since Raman bands are non-gaussian [6,72,73], such a data interpretation is purely qualitative but it still provides a piece of information on the connectivity of the glass network.

Table 2 shows the position, FWHM and relative area of the Q^n species and of the Fe^{3+} peak. Decreasing the alkali content from B1 to B4, the relative area between Q^1 and Q^2 decreases. Conversely, Q^3 shows a slight increase from B1 to B2, a similar value in B2 and B3 and a decrease in B4. Finally, the relative area of the Q^4 peaks results almost constant in B1, B2 and B3, but 8 times greater in B4. The area of the Fe^{3+} band mirrors the relative abundance of the trivalent Fe species in the total high-ω bell. As a matter of fact, comparing the Fe^{3+} band area to the weight percentage of Fe_2O_3 formed at 1770 K at 1 atm and recalculated using the Mössbauer data), it is possible to observe that the two indexes increase approximately together. However, the value of the Fe^{3+} relative area increases more rapidly than that of the Fe_2O_3 if compared to the total iron present in the glass. Considering the possible effect of Fe^{3+}, expressed by its relative integrated band area at 970 cm^{-1}, in the glass transition temperature, both Fe^{3+} band area and T_g look related in a linear fashion even though the errors produced by the fitting procedure are pretty high. This last issue is probably related to the number of gaussian used for the fitting and to the well-known overlapping effects. This finding is in line with the study of Ref. [49], in which the addition of iron to a binary sodium-silicate glass increases both the T_g and the Q^3 units in the glass.

	B1	B2	B3	B4	E122
Position (cm^{-1})					
Q^1	889	881	880	887	880
Q^2	920	921	920	921	915
Fe^{3+}	971	969	969	968	970
Q^3	1057	1056	1060	1055	1053
Q^4	1147	1158	1155	1153	1155
FWHM (cm^{-1})					
Q^1	47	40	46	45	47
Q^2	82	63	71	79	73
Fe^{3+}	100	110	103	101	103
Q^3	102	129	118	115	117
Q^4	98	75	80	87	94
Relative Area					
Q^1	0.08	0.06	0.05	0.04	0.04
Q^2	0.19	0.13	0.11	0.08	0.18
Fe^{3+}	0.39	0.42	0.43	0.45	0.43
Q^3	0.31	0.31	0.32	0.32	0.30
Q^4	0.04	0.08	0.09	0.10	0.05

286   **Table 2.** Results of the deconvolution procedure of the high-ω band. The contributions are fitted with Gaussian functions.
287   Table shows the peak position (cm^{-1}, error is <4 cm^{-1}); and the full width at half maximum (FWHM, cm^{-1}, error <7 cm^{-1}
288   $^{-1}$) and the peak area (arbitrary units, the relative error is < 15%).
289

290   The parameter Q_r defined as:

$$Q_r = Fe^{3+}/(Q^3+Q^2) \qquad (2)$$

291   Hence the ratio of the Fe^{3+} band, with respect to the Q^2 and Q^3 units. It describes the vibrational
292   contribution of the total Fe^{3+} ions (Fe^{3+}-O) in form of Fe_2O_3 with respect to the remaining symmetric
293   stretching vibrations of $Si_2O_6^{4-}$ and $Si_2O_5^{2-}$ structural units [68]. A similar approach was adopted in
294   Ref. [65] where the Q^2/Q^3 ratio (measured as spectral amplitude at the frequency maximum) is
295   linearly correlated with the Fe_2O_3 content. Figure 4 reports the relationship between the Q_r parameter,
296   the Fe_2O_3 recalculated according to Mössbauer data (expressed in normalized mol. %) and T_g.
297
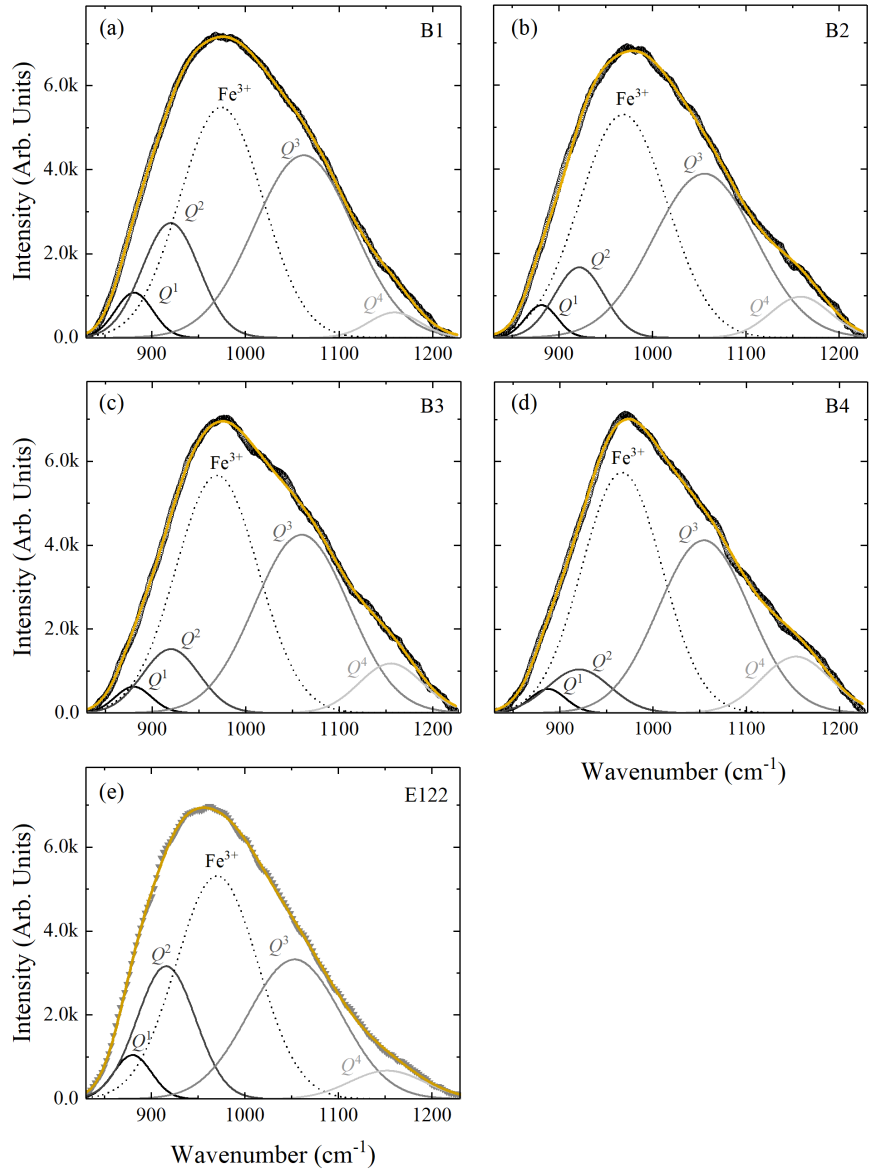
Figure 3 Deconvolution procedure of the high-ω region of HH polarized and Long-corrected Raman spectra of B1, B2, B3, B4 and E122 glasses, reported in panels (a), (b), (c), (d) and (e) respectively. The yellow lines are the cumulative fitting curves from the Gaussian components Q^1, Q^2, Q^3, Q^4 and Fe^{3+} band.
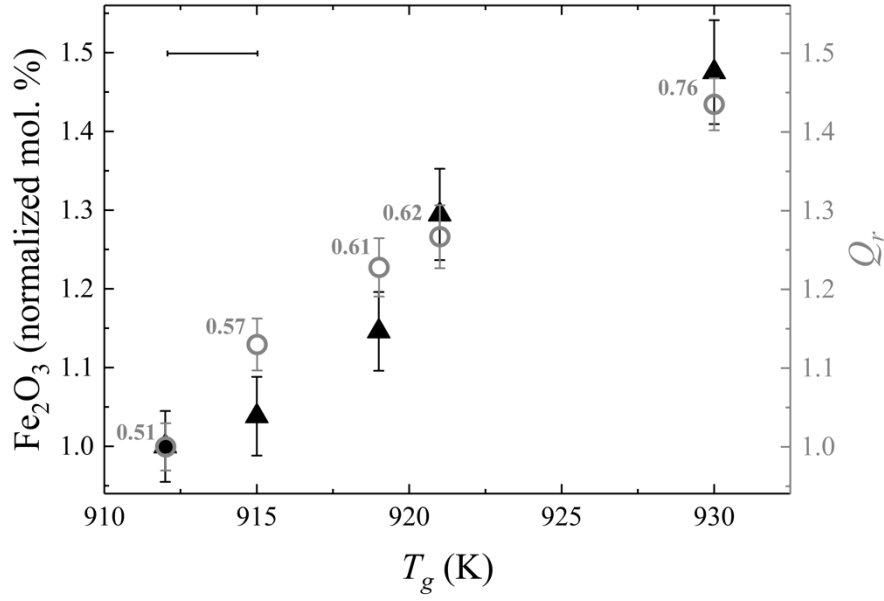
311   The analysis of the BP is done in HV cross-polarization since it suppresses the strongly

312 polarized R band that can mask the low-ω modes. Raw data show a strong contribution due to the air

313 rotational Raman modes. These features were carefully subtracted to gain air-free spectra.

314 Furthermore, a linear baseline was subtracted to remove the weak luminescence and the background.

315 The so obtained spectra were interpreted according to the Shuker and Gammon approach [74]. Thus,

316 the experimental intensity I^{exp} can be expressed as reduced intensity I^{red}, as:

$$I^{red}(\omega) = \frac{I^{exp}}{\omega\,[n(\omega,T)+1]} = C(\omega)\frac{g(\omega)}{\omega^2} \qquad (4)$$

317 where $n(\omega,T)= [\exp(\hbar\omega/k_BT)-1]^{-1}$ is the Bose-Einstein population factor $n(\omega,T)$, with k_B indicating

318 the Boltzmann constant, $\hbar$ is the reduced Planck's constant, T the absolute temperature in kelvin, and

319 $C(\omega)$ is the light-vibrations coupling function. Fig. 5 (a) reports the reduced low-ω spectra normalized

320 to the integrated area of the high-ω region, as reported in the inset. The band at ~ 970 cm^{-1} turns out

321 strongly depolarized (see Ref. [75]) and this is the result of bridging oxygens involved in the T-O-T

322 antisymmetric stretching within the glass network. Figure 5 (a,b) also reports the reduced Raman

323 intensity of the E122 sample. For $\omega \lesssim 20$ cm^{-1}, spectra show an increasing intensity due to the quasi-

324 elastic scattering (QES).

325   The BP maximum frequency ω_{BP} has been determined by fitting the low-ω reduced spectrum

326   to a log-normal function in the form $I(\omega) \propto \exp\{-[\ln(\omega/\omega_{BP})]^2/2\sigma^2\}$, where σ is the BP width and

327   ω_{BP} is the position of its maximum in cm^{-1} [76]. The fit starts from the lowest limit for the QES

328   intensity ($\sim 25\ cm^{-1}$), whose minima kink is very shortly extended below its low-ω tail (without

329   overlapping the BP), to $175\ cm^{-1}$ (see Fig. 5 (a)). The observed shift of ω_{BP} ranges between 63.5 (B4)

330   to 75.9 (B1) cm^{-1} and the intensity decreases of $\sim 37\%$.

331   Spectra can be compared by adopting the variable transformation $v = \omega/\omega_S$ and assuming

332    $g(v)dv = g(\omega)d\omega$ where $C(\omega) \propto \omega$ in the BP range [77,78]. Following, the rescaled intensity can be

333   written as:

$$I^{red}(v) = I^{red}(\omega)\ \omega_S^2 \qquad\qquad (5)$$

334   where ω_S is the squeezing frequency (*i.e.*, the frequency that rescales each spectrum to the same given

335   peak intensity [6,48]). The results of the scaling procedure are reported in Fig. 5 (b). Below $\sim 20\ cm^{-}$

336   ^{1}, the QES tail of the squeezed spectra exhibits the same behaviour of the unscaled spectra and

337   discussed before. Above the frequency of the QES minima, the scaling procedure seems to work

338   remarkably well up to the BP maxima. Increasing further the frequency, *i.e.* on the high frequency

339   tail of the BP, the distribution of the squeezed spectra results broader and sharper as the alkali content

340   increases or the $FeO_{(t)}$ content decreases. This produces a small excess wing behaviour as observed

341   in Ref. [46]. Conversely, the apparent decrease of the BP intensity in the four basalt-like glasses is

342   only apparent and it is related to the peak shift as the alkali oxides content decreases or the $FeO_{(t)}$ one

343   increases. This means that the elastic properties of basaltic glasses are conserved while the

344   microscopic structure is slightly modified by the different compositions.

$$\nu = \omega / \omega_s$$
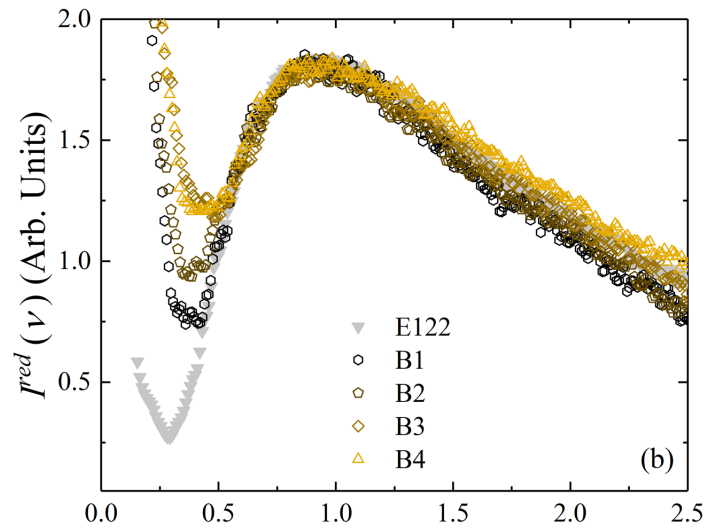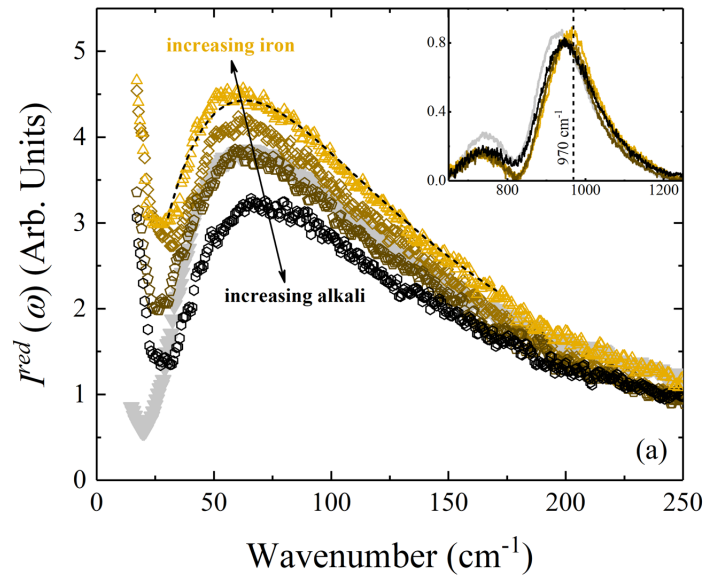
Figure 5 (a) Reduced intensity of the HV Raman spectra in the low-ω region. The black arrows are guides for the eye to mark the directions of the decreasing alkali contents and of the increasing contents. The inset shows the spectra normalzation using the integrated area of the high-ω HV bands. (b) Results of the scaling procedure of the BP.

Results show a correlation between vibrational properties, namely Q_r and ω_{BP}, and are linked to the calorimetric T_g which are in turn influenced by the iron-alkali substitution. This relation is shown in Figure 6.

353
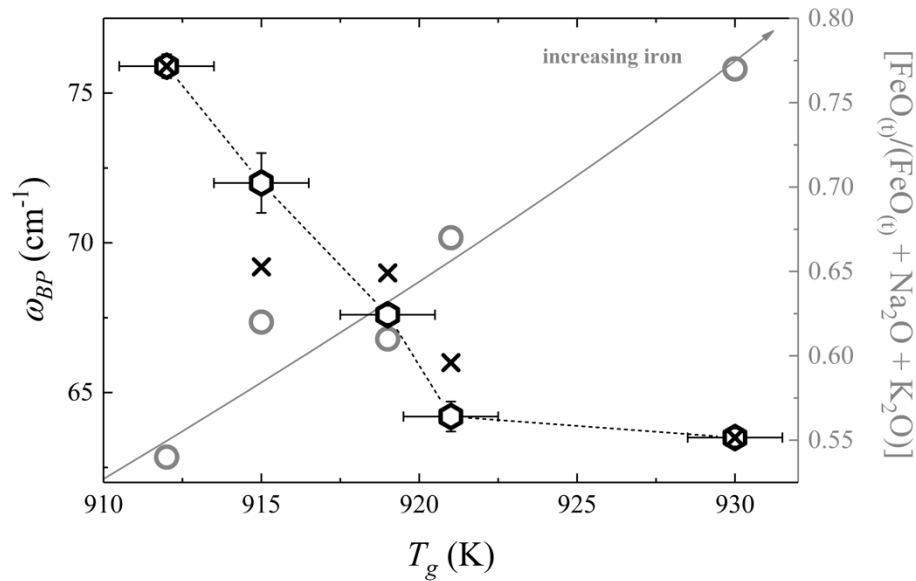
Figure 6 Relationship between the T_g and ω_{BP} (black hexagons) obtained by fitting the low-ω region to a log-normal function as explained in the text. The values of ω_S (black crosses) are also reported. The $FeO_{(t)}$ to alkali oxides ratio expressed by the parameter $[FeO_{(t)}/(FeO_{(t)}+Na_2O+K_2O)]$ is displayed in the secondary axis and reported as red circles. The black dashed line and the red arrow are guides for the eye.

Indeed, the slight variations of the R, D_1 and D_2 bands provides only marginal clues about the relative number of interconnected corner-sharing SiO_4 tetrahedra as well as on the small modifications of the T-O-T bond-angle distribution. However, results of the high-ω region deconvolution seem to be related to the calorimetric data, where the distribution of the Q^n species mirror the polymerization degree of the glass. In particular, the area of Q^2 slightly increases with ω_{BP}. This trend was already observed in Ref. [79] and could be due to an increasing distortion of the tetrahedral units [80]. Moreover, such small variations of Q^2 suggest that Fe^{2+} acts as NM Fe-poor and alkali-rich samples are more depolymerized than Fe-rich and alkali-poor ones. As $FeO_{(t)}$ increases, the area of the Q^3 and Fe^{3+} bands increase thus suggesting an evident stiffening of the glass structure. All together the small variations of the Q^n are generally derived by a gaussian deconvolution procedure which is, however, not representative of their nature [6,72]. Therefore, results would be consistent if validated with other technique (*i.e.*, by nuclear magnetic resonance [59]).

When compared to the thermal properties of glasses expressed by T_g, the BP shows a behaviour similar to that observed in Ref. [6]. Indeed, both its intensity decrease and frequency increase are accompanied by a lowering of the T_g, which is due to the reduction of the iron-alkali ratio (see Fig. 6). The values of the *adjustable parameter* ω_S are reported in the same plot with a cross symbol, and its slight variation denotes that the vibrational modes responsible for the BP are the same in B1 and B4 and slightly different in B2 and B3 glasses.

15

376   The variation of the BP can be ascribed to a hardening of the elastic medium due to a small

377   reorganization of the glass structure in the medium range order region. This idea is supported by the

378   scaling procedure shown in Fig. 5(b) and by the existence of a master curve. The iron-alkali

379   replacement in these basalts does not influences the properties of the elastic medium and their effects

380   is confined to small variation in the structure [6,48]. The small increase of the shape of the BP high-

381   frequency tails could be probably the effect of the data treatment (*i.e.*, background subtraction or

382   normalization to the high frequency region of the HV spectra, being in turn influenced by the short

383   rang order) but it could suggest the presence of further modes above the BP region. This aspect

384   deserves further investigation. When the E122 glass is introduced in the analysis, it scales notably

385   with the basaltic series. Even though the top of the different BPs collapses on each other, the low

386   frequency tail results broader and much more depressed in the minima point with respect to the

387   basaltic series ones. However, the high frequency tail of E122 scales notably with that of glass B2.

388

389

390   *Conclusion*

391

392   We investigated the thermal and vibrational properties of a set of basalt-like glasses with

393   different alkali and iron oxides content in a composition interval extremely interesting for the

394   production of glass fibres from natural material. The relative variation of alkali and iron oxides shows

395   a decrease of the glass transition temperature and a modification of the interconnection between TO_4

396   tetrahedra in the glass matrix. The increase of the $FeO_{(t)}$ content is accompanied by an increase of the

397   T_g showing a softening of the elastic continuum observed by a downward shift of the BP. These

398   effects are related to the strong increase of Fe^{3+} ions in the glass network as confirmed by high-ω

399   Raman and Mössbauer data.

400   This study confirms how natural materials, whose properties are considered extremely

401   variable due to their composition, have a quite huge interval of stability and their compositional

402   variability can be used to tune macroscopic properties such as the glass transition temperature.

403   Moreover, the low frequency region provides a crucial tool in glassy materials

404   characterization. Thus, the result depicted here highlight the both the determination vibrational

405   density of states and scaling protocols of the boson peak as complementary points in characterizing

406   complex multicomponent glasses.

407

408

409

415

416 *References*

417 [1]   P. Papale, Strain-induced magma fragmentation in explosive eruptions., Nature. 397 (1999) 425–428.
418 [2]   D.B. Dingwell, Volcanic dilemma: Flow or blow?, Science (1979). 273 (1996) 1054.
419 [3]   B.O. Mysen, Relationships between silicate melt structure and petrologic processes, Earth Science Reviews.
420   (1990).
421 [4]   D.L. Morse, J.W. Evenson, Welcome to the Glass Age, Int. J. Appl. Glass Sci. 7 (2016) 409–412.
422 [5]   M. Bauchy, Deciphering the atomic genome of glasses by topological constraint theory and molecular
423   dynamics: A review, Comput. Mater. Sci. 159 (2019) 95–102.
424 [6]   M. Cassetta, M. Zanatta, M. Biesuz, M. Giarola, G. Mariotto, New insights about the role of Na–K ratio on the
425   vibrational dynamics of synthetic-basalt glasses, Journal of Raman Spectroscopy. (2022) 1–10.
426 [7]   B.O. Mysen, D. Virgo, F.A. Seifert, Redox equilibria of iron in alkaline earth silicate melts: relationships
427   between melt structure, oxygen fugacity, temperature and properties of iron-bearing silicate liquids., Am. Min.
428   69 (1984) 834–847.
429 [8]   M. Wilke, Fe in magma - An overview, Ann. Geophys. 48 (2005) 609–617.
430 [9]   A. Borisov, H. Behrens, F. Holtz, Effects of strong network modifiers on Fe^{3+}/Fe^{2+} in silicate melts: an
431   experimental study, Contrib. Mineral. and Petrol. 172 (2017) 0.
432 [10] F. Farges, Y. Lefrère, S. Rossano, A. Berthereau, G. Calas, G.E. Brown, The effect of redox state on the local
433   structural environment of iron in silicate glasses: A combined XAFS spectroscopy, molecular dynamics, and
434   bond valence study, J. Non. Cryst. Solids. 344 (2004) 176–188.
435 [11] D.B. Dingwell, D. Virgo, The effect of oxidation state on the viscosity of melts in the system Na_2O-FeO-Fe_2O_3-
436   SiO_2, Geochim. Cosmochim. Acta. 51 (1987) 195–205.
437 [12] C. Liebske, H. Behrens, F. Holtz, R.A. Lange, The influence pf pressure and composition on the viscosity of
438   andesitic melts, Geochim. Cosmochim. Acta. 67 (2003) 473–485.
439 [13] D. Di Genova, K.U. Hess, M.O. Chevrel, D.B. Dingwell, Models for the estimation of Fe^{3+}/Fe_{tot} ratio in
440   terrestrial and extraterrestrial alkali- and iron-rich silicate glasses using Raman spectroscopy, American
441   Mineralogist. 101 (2016) 943–952.
442 [14] S. Kremers, Y. Lavallée, J. Hanson, K.U. Hess, M.O. Chevrel, J. Wassermann, D.B. Dingwell, Shallow
443   magma-mingling-driven Strombolian eruptions at Mt. Yasur volcano, Vanuatu, Geophys. Res. Lett. 39 (2012)
444   1–6.
445 [15] G. Calas, J. Petiau, Coordinationof Iron in oxide Glasses through High-Resolution K-Edge Spectra: Information
446   from the Pre-Edge, Solid State Commun. 48 (1983) 625–629.
447 [16] C. Weigel, L. Cormier, G. Calas, L. Galoisy, D.T. Bowron, Nature and distribution of iron sites in a sodium
448   silicate glass investigated by neutron diffraction and EPSR simulation, J. Non Cryst. Solids. 354 (2008) 5378–
449   5385.
450 [17] C. Wright, S.J. Clarke, C.K. Howard, The environment of Fe^{2+}/Fe^{3+} cations in a soda-lime-silica glass, Phys.
451   Chem. Glas. 55 (2014) 243–252
452 [18] P.A. Bingham, O.M. Hannant, N. Reeves-Mclaren, M.C. Stennett, R.J. Hand, Selective behaviour of dilute Fe^{3+}
453   ions in silicate glasses: An Fe K-edge EXAFS and XANES study, J. Non Cryst. Solids. 387 (2014) 47–56.
454 [19] J. Liu, M. Chen, J. Yang, Z. Wu, Study on Mechanical Properties of Basalt Fibers Superior to E-glass Fibers
455   Study on Mechanical Properties of Basalt Fibers Superior to E-glass, J. Nat. Fibers. 00 (2020) 1–13.
456 [20] C.D.M. Dufresne, P.L. King, M. Darby Diar, K.M. Dalby, Effect of SiO_2, total FeO, Fe^{3+}/Fe^{2+}, and alkali
457   elements in basaltic glasses on mid-infrared spectra, Am. Min. 94 (2009) 1580–1590.
458 [21] A.J. Berry, H.S.C. O'Neill, K.D. Jayasuriya, S.J. Campbell, G.J. Foran, XANES calibrations for the oxidation
459   state of iron in a silicate glass, Am. Min. 88 (2003) 967–977.
460 [22] V. Magnien, D.R. Neuville, L. Cormier, B.O. Mysen, V. Briois, S. Belin, O. Pinet, P. Richet, Kinetics of iron
461   oxidation in silicate melts: A preliminary XANES study, Chem. Geol. 213 (2004) 253–263.
462 [23] M. Bonnin-Mosbah, N. Métrich, J. Susini, M. Salomé, D. Massare, B. Menez, Micro X-ray absorption near
463   edge structure at the sulfur and iron K-edges in natural silicate glasses, Spectrochim. Acta Part B At. Spectrosc.
464   57 (2002) 711–725.

465 [24] A. Di Muro, N. Métrich, M. Mercier, D. Giordano, D. Massare, G. Montagnac, Micro-Raman determination of
466 iron redox state in dry natural glasses: Application to peralkaline rhyolites and basalts, Chem. Geol. 259 (2009)
467 78–88.
468 [25] C. Le Losq, A.J. Berry, M.A. Kendrick, D.R. Neuville, H.S.C. O'Neill, Determination of the oxidation state of
469 iron in Mid-Ocean Ridge basalt glasses by Raman spectroscopy, Am. Min. 104 (2019) 1032–1042.
470 [26] M. Mercier, A. Di Muro, D. Giordano, N. Métrich, P. Lesne, M. Pichavant, B. Scaillet, R. Clocchiatti, G.
471 Montagnac, Influence of glass polymerisation and oxidation on micro-Raman water analysis in alumino-silicate
472 glasses, Geochim. Cosmochim. Acta. 73 (2009) 197–217.
473 [27] D. González-García, D. Giordano, J.K. Russell, D.B. Dingwell, A Raman spectroscopic tool to estimate
474 chemical composition of natural volcanic glasses, Chem. Geol. 556 (2020)
475 [28] D. Di Genova, D. Morgavi, K.U. Hess, D.R. Neuville, N. Borovkov, D. Perugini, D.B. Dingwell, Approximate
476 chemical analysis of volcanic glasses using Raman spectroscopy, J. Raman Spectrosc. 46 (2015) 1235–1244.
477 [29] P. McMillan, Structural studies of silicate glasses and melts-applications and limitations of Raman
478 spectroscopy., Am. Min. 69 (1984) 622–644.
479 [30] P. Benassi, A. Fontana, W. Frizzera, M. Montagna, V. Mazzacurati, G. Signorelli, Disorder-induced light
480 scattering in solids: The origin of the boson peak in glasses, Philos. Mag. 71 (1995) 761–769.
481 [31] W. Götze, M.R. Mayr, Evolution of vibrational excitations in glassy systems, Phys. Rev. E. 61 (2000) 587–606.
482 [32] B. Schmid, W. Schirmacher, Raman scattering and the low-frequency vibrational spectrum of glasses, Phys.
483 Rev. Lett. 100 (2008) 1–4.
484 [33] A.J. Dianoux, U. Buchenau, M. Prager, N. Nücker, Low frequency excitations in vitreous silica, Phys. B. 138
485 (1986) 264–268. https://doi.org/10.1016/0378-4363(86)90006-9.
486 [34] E. Duval, A. Boukenter, T. Achibat, Vibrational dynamics and the structure of glasses, J. Phys. Condens.
487 Matter. 2 (1990) 10227–10234.
488 [35] T.S. Grigera, V. Martín-Mayor, G. Parisi, P. Verrocchio, Phonon interpretation of the "boson peak" in
489 supercooled liquids, Nature. 422 (2003) 289–292.
490 [36] M. Cassetta, D. Di Genova, M. Zanatta, T. Boffa Ballaran, A. Kurnosov, M. Giarola, G. Mariotto, Estimating
491 the viscosity of volcanic melts from the vibrational properties of their parental glasses, Sci Rep. 11 (2021)
492 13072.
493 [37] A.I. Chumakov, G. Monaco, A. Monaco, W.A. Crichton, A. Bosak, R. Rüffer, A. Meyer, F. Kargl, L. Comez,
494 D. Fioretto, H. Giefers, S. Roitsch, G. Wortmann, M.H. Manghnani, A. Hushur, Q. Williams, J. Balogh, K.
495 Parliński, P. Jochym, P. Piekarz, Equivalence of the boson peak in glasses to the transverse acoustic van, hove
496 singularity in crystals, Phys. Rev. Lett. 106 (2011) 1–5.
497 [38] M. Zanatta, G. Baldi, S. Caponi, A. Fontana, C. Petrillo, F. Rossi, F. Sacchetti, Debye to non-Debye scaling of
498 the Boson peak dynamics: Critical behavior and local disorder in vitreous germania, J. Chem. Phys. 135 (2011)
499 3–8.
500 [39] M. Zanatta, A. Fontana, F. Rossi, E. Gilioli, Effects of permanent densification on the vibrational density of
501 states of vitreous silica, J. Non Cryst. Solids. 357 (2011) 1892–1894.
502 [40] F. Rossi, G. Baldi, S. Caponi, R. Dal Maschio, A. Fontana, L. Orsingher, M. Zanatta, The vibrational dynamics
503 of GeO_2 at the glass transition: A Raman and Brillouin scattering study, Philos. Mag. 91 (2011) 1910–1916.
504 [41] N. Tomoshige, H. Mizuno, T. Mori, K. Kim, N. Matubayasi, Boson peak, elasticity, and glass transition
505 temperature in polymer glasses: Effects of the rigidity of chain bending, Sci. Rep. 9 (2019) 1–13.
506 [42] S. Caponi, A. Fontana, F. Rossi, G. Baldi, E. Fabiani, Effect of temperature on the vibrational density of states
507 in vitreous $SiO2$: A Raman study, Phys. Rev. B. 76 (2007) 1–4.
508 [43] G. Baldi, A. Fontana, F. Rossi, G. Monaco, Raman scattering investigation of the boson peak in a sodium
509 silicate glass, Philos. Mag. 91 (2011) 1801–1808.
510 [44] M.F. Ando, O. Benzine, Z. Pan, J.L. Garden, K. Wondraczek, S. Grimm, K. Schuster, L. Wondraczek, Boson
511 peak, heterogeneity and intermediate-range order in binary SiO_2-Al_2O_3 glasses, Sci. Rep. 8 (2018) 5394.
512 [45] Y. Matsuda, M. Kawashima, Y. Moriya, T. Yamada, O. Yamamuro, S. Kojima, Composition dependence of the
513 boson peak and universality in lithium borate binary glasses: Inelastic neutron and raman scattering studies, J.
514 Physical Soc. Japan. 79 (2010) 14–17.
515 [46] G. Baldi, A. Fontana, G. Monaco, Vibrational dynamics of non-crystalline solids, ArXiv. 2011 (2020) 10415.
516 [47] K. Niss, B. Begen, B. Frick, J. Ollivier, A. Beraud, A. Sokolov, V.N. Novikov, C. Alba-Simionesco, Influence
517 of pressure on the boson peak: Stronger than elastic medium transformation, Phys. Rev. Lett. 99 (2007) 3–6.
518 [48] M. Zanatta, G. Baldi, S. Caponi, A. Fontana, E. Gilioli, M. Krish, C. Masciovecchio, G. Monaco, L. Orsingher,
519 F. Rossi, G. Ruocco, R. Verbeni, Elastic properties of permanently densified silica: A Raman, Brillouin light,
520 and x-ray scattering study, Phys. Rev. B. 81 (2010) 4–7.
521 [49] E. Belova, Y.A. Kolyagin, I.A. Uspenskaya, Structure and glass transition temperature of sodium-silicate
522 glasses doped with iron, J. Non Cryst. Solids. 423–424 (2015) 50–57.
523 [50] P. Stabile, S. Sicola, G. Giuli, E. Paris, M.R.R. Carroll, J. Deubener, D. Di Genova, The effect of iron and alkali
524 on the nanocrystal-free viscosity of volcanic melts: A combined Raman spectroscopy and DSC study, Chem.
525 Geol. 559 (2021) 119991.
526 [51] M.G. Best, Igneous and Metamorphic Petrology, Blackwell Publishing Inc., 2003.

527   [52]   M. Coltelli, P. Del Carlo, L. Vezzoli, Discovery of a Plinian basaltic eruption of Roman age at Etna volcano,
528   Italy, Geology. 26 (1998) 1095–1098.

529   [53]   F. Vetere, F. Holtz, Rheological Behavior of Partly Crystallized Silicate Melts Under Variable Shear Rate,
530   Dynamic Magma Evolution, Geophysical Monograph, Wiley. 1 (2021) 152–167.

531   [54]   Q. Zheng, Y. Zhang, M. Montazerian, O. Gulbiten, J.C. Mauro, E.D. Zanotto, Y. Yue, Understanding Glass
532   through Differential Scanning Calorimetry, Chem. Rev. 119 (2019) 7848–7939.

533   [55]   D.G. Rancourt, Mössbauer spectroscopy in clay science, 1998.

534   [56]   K. Lagarec, D.G. Rancourt, Recoil User Manual Mössbauer spectral analysis software for Windows, 1st ed.,
535   University of Ottawa, Ottawa, 1998.

536   [57]   B.O. Mysen, D. Virgo, F.A. Seifert, Redox equilibria of iron in alkaline earth silicate melts: relationships
537   between melt structure, oxygen fugacity, temperature and properties of iron-bearing silicate liquids., Am. Min.
538   69 (1984) 834–847.

539   [58]   F.L. Galeener, Band limits and the vibrational spectra of tetrahedral glasses, Phys. Rev. B. 19 (1979) 4292–
540   4297.

541   [59]   C. Le Losq, D.R. Neuville, P. Florian, G.S. Henderson, D. Massiot, The role of Al^{3+} on rheology and structural
542   changes in sodium silicate and aluminosilicate glasses and melts, Geochim. Cosmochim. Acta. 126 (2014) 495–
543   517.

544   [60]   B.O. Mysen, L.W. Finger, D. Virgo, F.A. Seifert, Curve-fitting of Raman spectra of silicate glasses., Am. Min.
545   67 (1982) 686–695.

546   [61]   N. Zotov, Y. Yanev, M. Epelbaum, L. Konstantinov, Effect of water on the structure of rhyolite glasses - X-ray
547   diffraction and Raman spectroscopy studies, J. Non Cryst. Solids. 142 (1992) 234–246.

548   [62]   M. Okuno, N. Zotov, M. Schmücker, H. Schneider, Structure of SiO_2-Al_2O_3 glasses: Combined X-ray
549   diffraction, IR and Raman studies, J. Non Cryst. Solids. 351 (2005) 1032–1038.

550   [63]   M. Roskosz, M.J. Toplis, D.R. Neuville, B.O. Mysen, Quantification of the kinetics of iron oxidation in silicate
551   melts using Raman spectroscopy and assessment of the role of oxygen diffusion, Am. Min. 93 (2008) 1749–
552   1759.

553   [64]   A. Quaranta, A. Rahman, G. Mariotto, C. Maurizio, E. Trave, F. Gonella, E. Cattaruzza, E. Gibaudo, J.E.
554   Broquin, Spectroscopic investigation of structural rearrangements in silver ion-exchanged silicate glasses, J.
555   Phys. Chem. C. 116 (2012) 3757–3764.

556   [65]   B.O. Mysen, Role of Al in depolymerized, peralkaline aluminosilicate melts in the systems Li_2O-Al_2O_3-SiO_2,
557   Na_2O-Al_2O_3-SiO_2, and K_2O-Al_2O_3-SiO_2, Am. Min. 75 (1990) 120–134.

558   [66]   Z. Wang, T.F. Cooney, S.K. Sharma, In situ structural investigation of iron-containing silicate liquids and
559   glasses, Geochim. Cosmochim. Acta. 59 (1995) 1571–1577.

560   [67]   V. Magnien, D.R. Neuville, L. Cormier, J. Roux, J.L. Hazemann, O. Pinet, P. Richet, Kinetics of iron redox
561   reactions in silicate liquids: A high-temperature X-ray absorption and Raman spectroscopy study, J. Nucl.
562   Mater. 352 (2006) 190–195.

563   [68]   B.O. Mysen, F. Seifert, D. Virgo, Structure and redox equilibria of iron-bearing silicate melts, Am. Min. 65
564   (1980) 867–884.

565   [69]   K. Baert, W. Meulebroeck, H. Wouters, P. Cosyns, K. Nys, H. Thienpont, H. Terryn, Using Raman
566   spectroscopy as a tool for the detection of iron in glass, J. Raman Spectrosc. 42 (2011) 1789–1795.

567   [70]   M. Tarrago, I. Royo, S. Martínez, M. Garcia-Valles, D.R. Neuville, Incorporation of calcium in glasses: A key
568   to understand the vitrification of sewage sludge, Int. J. Appl. Glass. Sci. 12 (2021) 367–380.

569   [71]   A.M. Welsch, J.L. Knipping, H. Behrens, Fe-oxidation state in alkali-trisilicate glasses - A Raman
570   spectroscopic study, J. Non Cryst. Solids. 471 (2017) 28–38.

571   [72]   N. Zotov, I. Ebbsjö, D. Timpel, H. Keppler, Calculation of Raman spectra and vibrational properties of silicate
572   glasses: Comparison between $Na_2Si_4O_9$ and SiO_2 glasses, Phys. Rev. B. 60 (1999) 6383–6397.

573   [73]   W.J. Malfait, V.P. Zakaznova-Herzog, W.E. Halter, Quantitative Raman spectroscopy: Speciation of Na-silicate
574   glasses and melts, Am. Min. 93 (2008) 1505–1518.

575   [74]   R. Shuker, R.W. Gammon, Raman-scattering selection-rule breaking and the density of states in amorphous
576   materials, Phys. Rev. Lett. 25 (1970) 222–225.

577   [75]   Z. Wang, T.F. Cooney, S.K. Sharma, In situ structural investigation of iron-containing silicate liquids and
578   glasses, Geochim. Cosmochim. Acta. 59 (1995) 1571–1577.

579   [76]   V.K. Malinovsky, V.N. Novikov, A.P. Sokolov, Log-normal spectrum of low-energy vibrational excitations in
580   glasses, Phys. Lett. A. 153 (1991) 63–66.

581   [77]   A. Fontana, R. Dell'Anna, M. Montagna, F. Rossi, G. Viliani, G. Ruocco, M. Sampoli, U. Buchenau, A.
582   Wischnewski, The Raman coupling function in amorphous silica and the nature of the long-wavelength
583   excitations in disordered systems, Europhys. Lett. 47 (1999)

584   [78]   A. Fontana, F. Rossi, G. Viliani, S. Caponi, E. Fabiani, G. Baldi, G. Ruocco, R. Dal Maschio, The Raman
585   coupling function in disordered solids: A light and neutron scattering study on glasses of different fragility, J.
586   Phys. Condens. Matter. 19 (2007) 205145.

587   [79]   D.R. Neuville, Viscosity, structure and mixing in (Ca, Na) silicate melts, Chem. Geol. 229 (2006) 28–41.

588 [80] B. Hehlen, E. Courtens, A. Yamanaka, K. Inoue, Nature of the Boson peak of silica glasses from hyper-Raman
589   scattering, J. Non Cryst. Solids. 307–310 (2002) 87–91.
590
591